Journal of Solid State Chemistry 186 (2012) 1–8

Contents lists available at SciVerse ScienceDirect

Journal of Solid State Chemistry

journal homepage: www.elsevier.com/locate/jssc

Oxygen exchange on nanocrystalline tin dioxide modified by palladium

D.D. Frolov [a], Y.N. Kotovshchikov [a], I.V. Morozov [a], A.I. Boltalin [a], A.A. Fedorova [a], A.V. Marikutsa [a,*], M.N. Rumyantseva [a], A.M. Gaskov [a], E.M. Sadovskaya [b], A.M. Abakumov [c]

[a] Chemistry Department, Moscow State University, Moscow 119899, Russia
[b] Boreskov Institute of Catalysis, RAS, Novosibirsk 630090, Russia
[c] EMAT, University of Antwerp, Antwerp B-2020, Belgium

ARTICLE INFO

Article history:
Received 12 September 2011
Received in revised form
15 November 2011
Accepted 17 November 2011
Available online 28 November 2011

Keywords:
Nanocrystalline tin dioxide
Oxygen isotopic exchange
Oxygen diffusion
Heteroexchange
Palladium

ABSTRACT

Temperature-programmed oxygen isotopic exchange study was performed on nanocrystalline tin dioxide-based materials synthesized via sol–gel route and modified by palladium. Such materials are widely used as resistive gas sensors. The experiments were carried out in a flow-reactor up to complete isotopic substitution of oxygen. Substantial rates of isotopic exchange for SnO_2 were observed from about 700 K. The distribution of isotopic molecules $^{16}O_2$, $^{16}O^{18}O$ and $^{18}O_2$ corresponds to simple dioxygen heteroexchange mechanism with single lattice oxygen atom. The modification of SnO_2 by Pd introduced multiple heteroexchange mechanism with preliminary O_2 dissociation on the clusters surface. Spill-over of atomic oxygen from Pd to the surface of SnO_2 and fast exchange with lattice oxygen result in more than 100% increase of apparent heteroexchange rate. The exchange on SnO_2/Pd was shown to be a complex process involving partial deactivation of the catalytic centers at temperature higher than 750 K.

1. Introduction

Nanocrystalline tin dioxide based materials are widely applied in the field of semiconductor gas sensors due to high sensitivity to many pollutant gases at maximum permissible concentration level and the stability of the oxide materials at ambient conditions [1]. Modification of tin dioxide surface by Pd additive has been shown to improve the sensor performance, e.g. selectivity, sensitivity and optimal operation temperature interval, especially when the target gas to be detected possesses reductive properties, e.g. CO [2–4], CH_4, H_2, ethanol, acetone [4–6], etc. The sensor response of tin dioxide-based materials, determined by electric conductivity variation upon ambient gas composition changing [1], is concerned to be due to electron concentration controlling chemical reactions of oxygen-related species, e.g. O^{2-} from oxide bulk or chemisorbed O_2^- and O^- with target gas molecules. Such processes on the surface of sensing materials are interpreted similarly to the reactions on heterogeneous oxide catalysts. The latter ones could be of three general mechanisms [7]: (i) Langmuir–Hinshelwood mechanism where both the reactants are competitively chemisorbed on the catalyst surface; (ii) Rideal–Eley mechanism in which only one reactant is chemisorbed and the other comes directly from gas phase; (iii) Mars–van Krevelen mechanism involving bulk oxygen ions of oxide catalyst as one of the reactants. In the case of reductive gases sensing with SnO_2, the target gas oxidation by chemisorbed O^- and O_2^- species is believed to be the response forming process [1]. Raised temperature is usually needed (500–700 K or higher [8]) for such reactions. Several hypotheses are widely discussed to explain the Pd-promoted improvement of the sensor properties towards reductive gases detection, especially CO, e.g. direct target gas oxidation by oxidized Pd species [1,9], modulation of material electric properties via Pd^{2+} incorporation into the SnO_2 lattice [2], gas molecules spill-over on the PdO grain boundaries [9] and hydroxyl groups—Pd cooperation in the oxidation process [10,11]. The latter proposals regarding palladium influence on the oxygen-related species reactivity, in particular the spill-over and OH–Pd interplay should be interrelated with the influence of Pd on oxygen mobility. Hence, the comparative study of oxygen mobility in blank tin dioxide and Pd-modified SnO_2 could shed some light on the promotional effect of Pd on tin dioxide surface reactivity.

Oxygen isotopic exchange study is a powerful technique for the evaluation of oxygen mobility in heterogeneous catalysts of oxidation processes, e.g. transition metal oxides and oxide-supported noble metal particles [12,13], or in the oxygen conductive

* Corresponding author. Fax: +7 495 9390998.
E-mail addresses: morozov@inorg.chem.msu.ru (I.V. Morozov), artem.marikutsa@gmail.com (A.V. Marikutsa), roum@inorg.chem.msu.ru (M.N. Rumyantseva), gaskov@inorg.chem.msu.ru (A.M. Gaskov), sadovsk@catalysis.ru (E.M. Sadovskaya), Artem.Abakumov@ua.ac.be (A.M. Abakumov).

0022-4596/$ - see front matter © 2011 Elsevier Inc. All rights reserved.
doi:10.1016/j.jssc.2011.11.028

materials for electrochemical applications (YSZ, CeO_2–ZrO_2, etc.). The experiments on isotopic exchange can be performed in static [14,15] or flow conditions [12,13], with theoretical simulation of the derived data providing an insight into the oxygen exchange mechanism, kinetic parameters of the processes (rate, activation energies and diffusion coefficients) and exchangeable oxygen fraction.

In this paper we present temperature-programmed oxygen isotopic exchange (TPIE) study of nanocrystalline SnO_2 materials, both blank and modified by Pd. The main objective of this work is to estimate the oxygen exchange ability of SnO_2-based materials as they are used for gas sensors with particular attention to the influence of the modification of SnO_2 surface by Pd on the oxygen exchange behavior.

2. Materials and methods

2.1. Synthesis of nanocrystalline SnO_2 and its modification by Pd

Nanocrystalline SnO_2 was synthesized via aqueous precipitation route as we previously described in [11]. The obtained $SnO_2 \cdot nH_2O$ powder was annealed at 573 K for 24 h. The resultant nanocrystalline SnO_2 sample was used both for further measurements and for modification by Pd.

The modification of SnO_2 was carried out via an impregnation method also described in [11]. The nominal quantity of the modifier was 1 wt% of Pd. The impregnated SnO_2/$Pd(acac)_2$ subproduct was calcined at 498 K for 24 h, the lowest temperature of $Pd(acac)_2$ decomposition evidenced by TG-DSC (Fig. 1).

2.2. Materials characterization

Phase composition and crystal structure were examined by X-ray diffraction with the DRON-3M instrument. The crystallite size (d_{XRD}) of SnO_2 was calculated from the broadening of (110) XRD peak using the Scherer equation, wave length $\lambda = 1.54051$ Å ($CuK\alpha_1$ radiation). The microstructure of the samples was characterized by high resolution transmission electron microscopy (HRTEM), high angle annular dark field scanning transmission electron microscopy (HAADF-STEM) and energy-dispersive X-ray (EDX) analysis with a Tecnai G2 transmission electron microscope operated at 200 kV. The specific surface area of powders was measured by nitrogen adsorption method using the BET model with the Chemisorb 2750 instrument (Micromeritics).

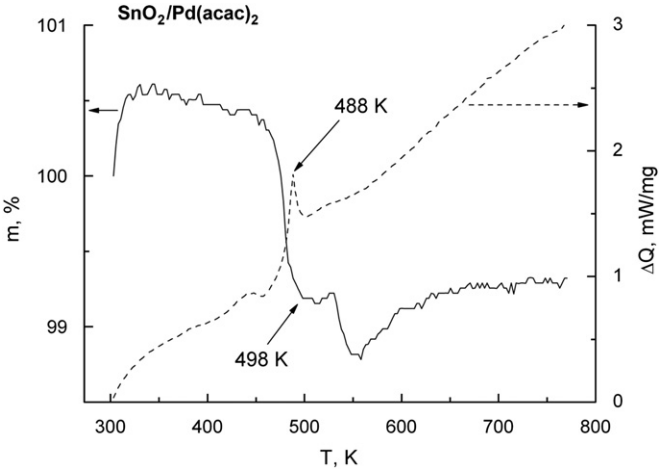

Fig. 1. TG-DSC spectra of the Pd-precursor decomposition in impregnated SnO_2/$Pd(acac)_2$ subproduct. Left axis—sample mass (percent of the initial mass); right axis—heat difference (mW per 1 mg of sample).

Characterization of surface species of the samples was carried out by means of Temperature Programmed Reduction by H_2 (TPR-H_2) using the Chemisorb 2750 (Micromeritics) instrument. The powders were tested without a pretreatment. The test gas used was 10 vol% H_2 in argon, gas flow rate 10 ml/min, heating from room temperature to 1073 K with the rate 10 K/min.

2.3. Study of oxygen isotopic exchange

The experiments on the oxygen isotopic exchange were performed in a temperature-programmed isotopic exchange (TPIE) mode. The experimental setup included source for test gas, namely Ar and $^{16}O_2$ (both analytical pure grade) and the electrolyzer filled with water with high concentration of $H_2^{18}O$ as a source of an equilibrium mixture of $^{18}O_2$, $^{16}O^{18}O$ and $^{18}O_2$ molecules. The desired test gas composition containing Ar, $^{16}O_2$, $^{16}O^{18}O$ and $^{18}O_2$ was controlled by mass-flow controller. Total gas flow rate was about 20 ml/min, with the overall oxygen content of 25%. The test gas was passed through a reactor (quartz tube, length 230 mm, diameter 13 mm) placed inside a tube furnace. Samples were heated up to 1073 K with the rate 200 K/h. The powders (about 0.9 g) were put on a porous silica membrane inside the reactor. A part of the outlet gas flow was taken to the mass-spectrometer and the ion current at mass numbers 32 ($^{16}O_2$), 34 ($^{16}O^{18}O$) and 36 ($^{18}O_2$) were recorded together with sample temperature measured by a thermocouple. The molecular oxygen fractions were calculated from the raw data by the following equations:

$$f_{32} = \frac{I_{32}}{I_{32}+I_{34}+I_{36}}, \quad (1)$$

$$f_{34} = \frac{I_{34}}{I_{32}+I_{34}+I_{36}}, \quad (2)$$

$$f_{36} = \frac{I_{36}}{I_{32}+I_{34}+I_{36}}, \quad (3)$$

where I_{32}, I_{34} and I_{36} are the ion currents at mass numbers 32, 34 and 36. The atomic fraction of ^{18}O in the test gas was calculated from molecular oxygen fractions using the equation:

$$\alpha = \frac{f_{34}}{2} + f_{36}. \quad (4)$$

The blank SnO_2 sample was examined by the so called equilibrated test gas mixture, i.e. containing 46% of $^{16}O^{18}O$, 41% of $^{18}O_2$ and 13% of $^{16}O_2$ that corresponds to the statistical distribution of isotopes. This sample was pretreated in the reactor by heating up to 573 K for 1 h in the Ar flow, holding at 573 K for 2 h and cooling down to 473 K for 1 h at the $^{16}O_2$ flow. The SnO_2/Pd sample was used without the pretreatment to prevent undesired morphologic changes and tested by non-equilibrium test gas mixture containing 15% of $^{16}O^{18}O$, 40% of $^{18}O_2$ and 45% of $^{16}O_2$ from the total O_2 content.

3. Results and discussion

3.1. Materials composition and microstructure

For the sake of comparison we investigated the phase composition and microstructure parameters of blank and Pd-modified tin dioxide as prepared (denoted as SnO_2 and SnO_2/Pd) and after the temperature-programmed isotopic exchange experiments (denoted as SnO_2-TPIE and SnO_2/Pd-TPIE, respectively). The X-ray diffraction patterns of the samples are shown in Fig. 2. The phase evaluation revealed nanocrystalline cassiterite (SnO_2) phase. No palladium-related species were detected by XRD due to either small Pd content or additive segregation or clustering on the

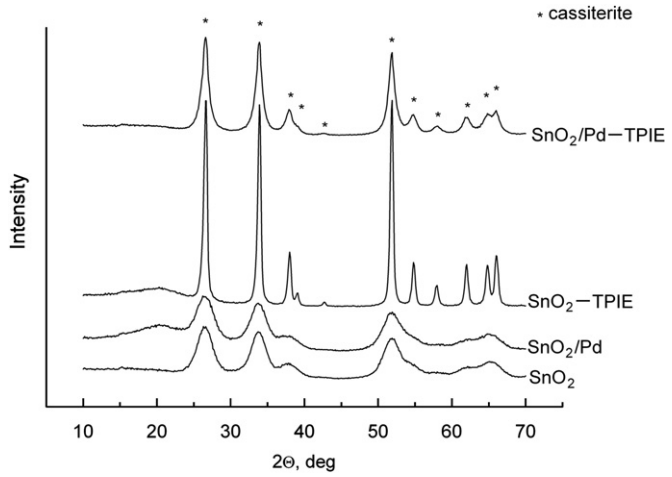

Fig. 2. XRD patterns of blank tin dioxide (curve SnO_2), palladium-modified SnO_2 (curve SnO_2/Pd), SnO_2 after TPIE experiment (curve SnO_2-TPIE) and SnO_2/Pd after TPIE experiment (curve SnO_2/Pd-TPIE).

surface of tin dioxide grains. However, the same observation was made on analogous Pd-modified materials in our previous work [11] where the modifier was proved by XPS to occur in a mixed Pd/PdO form. In the present work such sample is designated as SnO_2/Pd for simplicity. The average particle size (d_{XRD}) calculated using the Scherer equation was 2–5 nm for as prepared SnO_2 and SnO_2/Pd. Their BET specific surface area was about 90–95 m^2/g. The modifying of tin dioxide by palladium had no observable effect on the crystallite size and surface area of as prepared samples. Low magnification TEM images (Fig. 3a) and HRTEM images (Fig. 3b) of the as prepared samples revealed agglomerated irregularly shaped tin dioxide particles with a size ranging from 3 nm to 10 nm, which is in accordance with the calculations of d_{XRD}. Electron diffraction pattern indicates that SnO_2 is the only crystalline phase in the samples (Fig. 3a). A small amount of palladium (about 1 wt%) was detected in the EDX spectra of agglomerated particles, but HAADF-STEM did not visualize any Pd segregation presumably due to small modifier concentration and/or its homogeneous distribution (Fig. S1 of Supporting Information). It should be noted that occurrence of Pd on the surface of the SnO_2 particles strongly depends on the particle size. If Pd is deposited on coarse crystalline SnO_2 particles with the size of 15–100 nm prepared at 970 K, clear clustering of Pd into nanoparticles of 5–10 nm is observed (Fig. S2 of Supporting Information). Such clustering is definitely absent in the SnO_2/Pd sample prepared at 573 K, suggesting more homogeneous Pd distribution over the surface of the particles. The origin of this difference will be the subject of forthcoming publication.

Since during the TPIE experiments the samples were heated up to 1073 K, they underwent drastic morphologic changes resulted in sintering the crystallites evidenced by XRD (Fig. 2) and HRTEM. Yet, the degree of sintering turned to be different for the samples: the d_{XRD} values were 17–19 nm for the SnO_2-TPIE and 7–10 nm for the SnO_2/Pd-TPIE samples. The crystallite sizes estimated from HRTEM micrographs were 30–50 nm for the SnO_2-TPIE and 10–20 nm for the SnO_2/Pd-TPIE samples (Fig. 4a). The BET area was estimated to about 5–10 m^2/g for SnO_2-TPIE and 20–25 m^2/g for the SnO_2/Pd-TPIE samples. Thus, the modifier is likely to prevent tin dioxide grains from sintering to such a large extent as it was in the case of blank SnO_2. This could be due to Pd-induced inhibition of the surface diffusion and particles restructuring of tin dioxide as discussed in [16]. Regarding the Pd restructuring upon heating, no clear modifier segregation could be observed by HAADF-STEM imaging combined with EDX mapping of the SnO_2/Pd-TPIE sample. However, recording the EDX

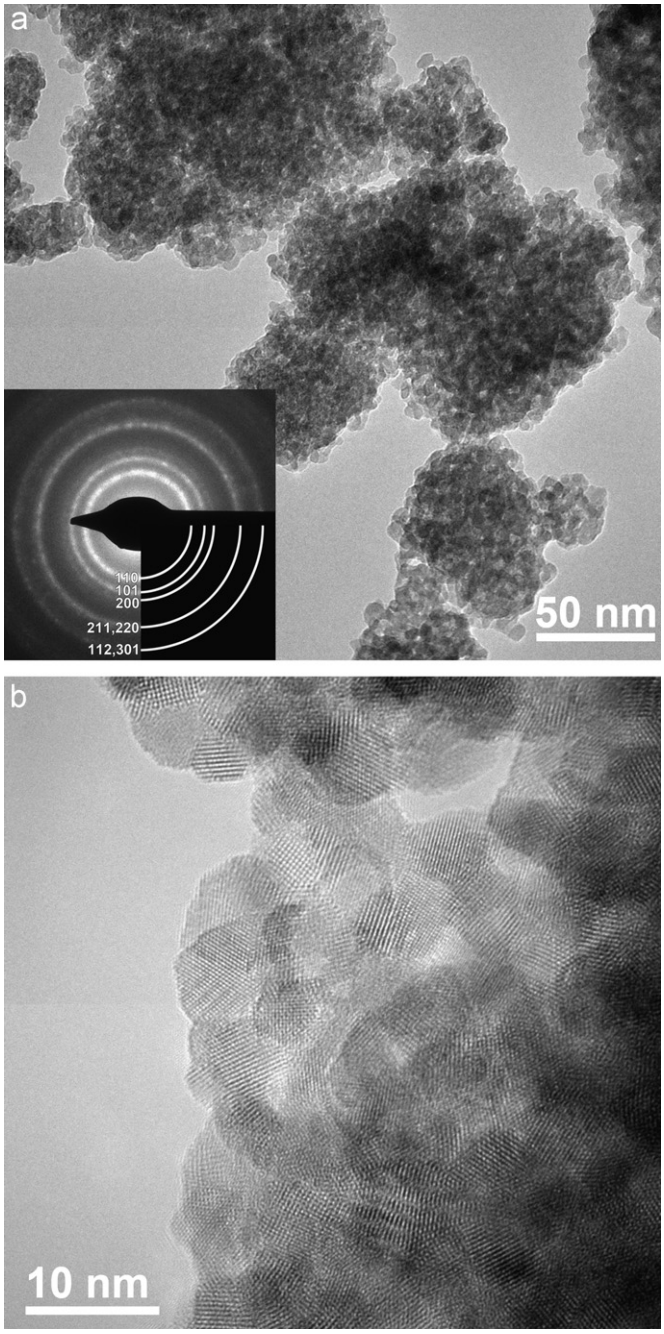

Fig. 3. (a) Low magnification TEM image of the SnO_2/Pd sample; inset—the electron diffraction pattern with the diffraction rings indexed according to the cassiterite structure. (b) High-resolution micrograph of the SnO_2/Pd sample.

spectra from different areas (50–100 nm sized squares) of the sample for a long time revealed large-scale inhomogeneous Pd distribution suggested by its concentration variations from noise level to 1.9 wt% for different regions (Fig. 4b and c). Hence, the only observed effect of high-temperature treatment during TPIE experiment on the Pd microstructure was the transition from nearly homogeneous to highly inhomogeneous distribution in the sample. This could arise from palladium decoration by tin dioxide and temperature-induced diffusion and sintering of the decorated Pd species.

To evaluate the content of the surface species in the samples before and after the TPIE experiments, temperature-programmed reduction by H_2 was performed. The TPR-spectra of as prepared SnO_2 (Fig. 5a) and SnO_2/Pd (Fig. 5b) are characterized by two

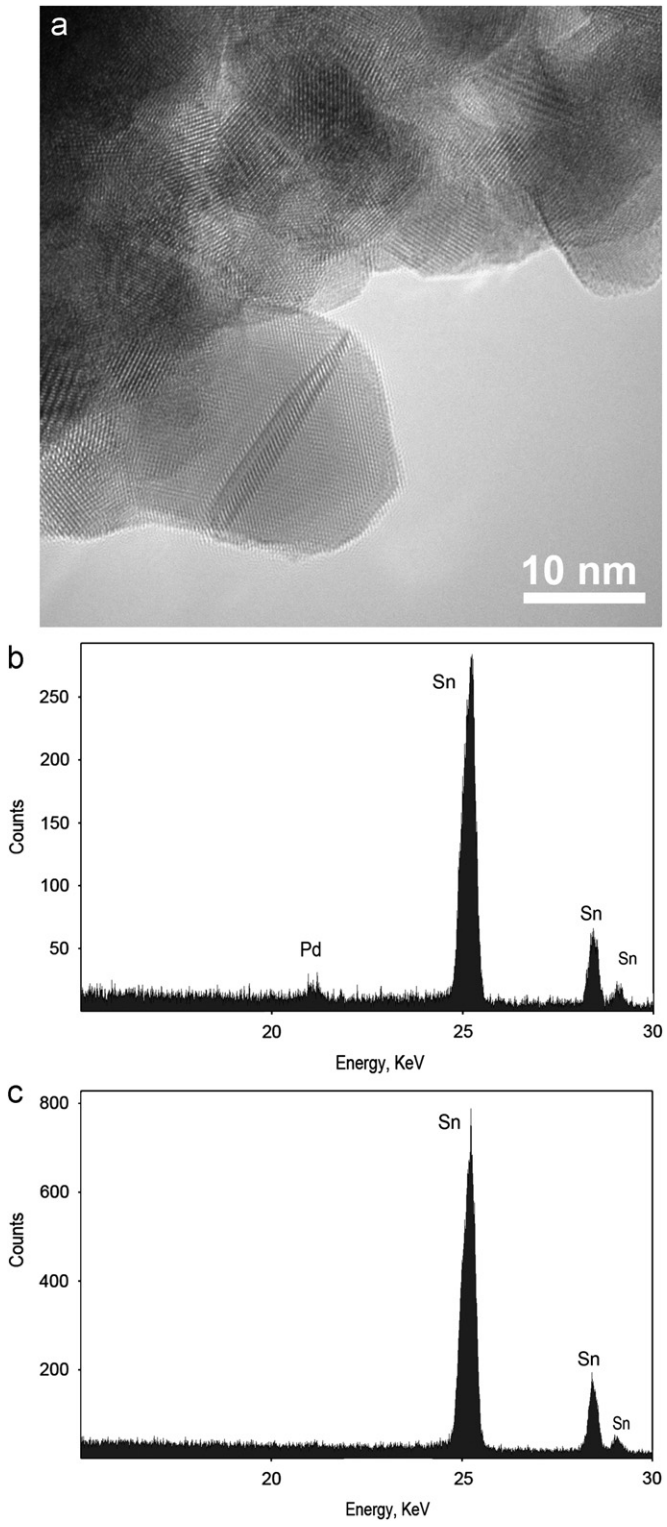

Fig. 4. (a) High-resolution micrograph of the SnO_2/Pd-TPIE sample; (b, c) EDX spectra of the different 50–100 nm areas demonstrating presence and absence of Pd, respectively.

H_2-consumption broad peaks: the smaller one at lower temperature (370–570 K) and the stronger one at higher temperature (720–920 K). The first peak is attributed to H_2 consumption during the reduction of surface species, i.e. O^-, O_2^- and OH groups [11]:

$$O^-_{(surf)} + H_{2(g)} = H_2O_{(g)} + e^-; \quad (5)$$

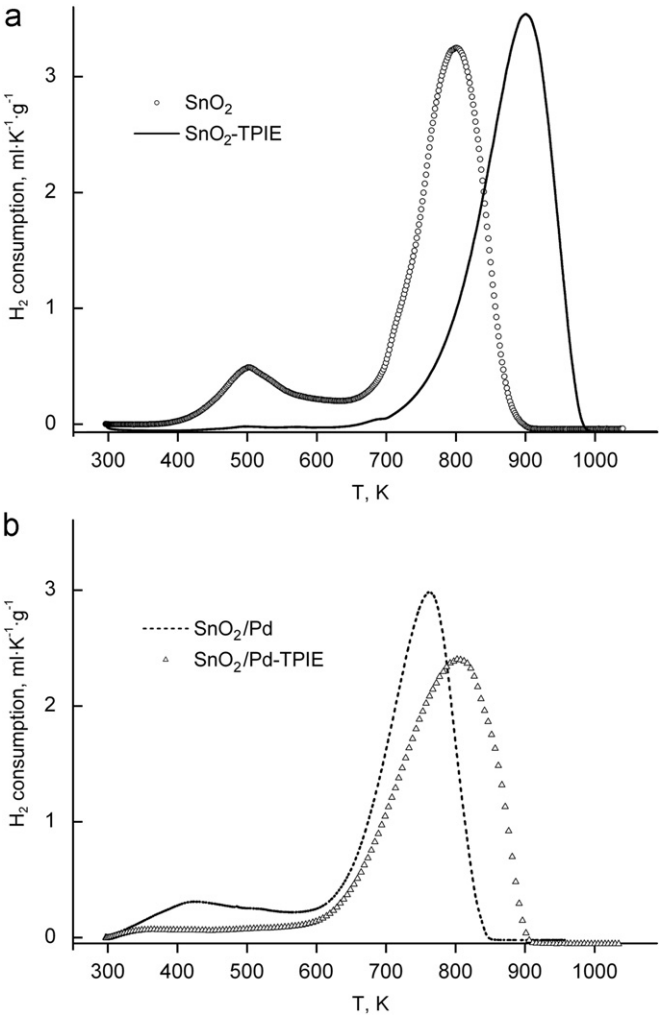

Fig. 5. TPR-H_2 spectra of as prepared (a) and TPIE-tested (b) SnO_2 and SnO_2/Pd samples.

$$O^-_{2(surf)} + 2H_{2(g)} = 2H_2O_{(g)} + e^-; \quad (6)$$

$$2OH_{(surf)} + H_{2(g)} = 2H_2O_{(g)}. \quad (7)$$

The high-temperature H_2 consumption is assigned to SnO_2 bulk reduction according to [11]:

$$SnO_{2(s)} + 2H_{2(g)} = Sn_{(s)} + 2H_2O_{(g)}; \quad (8)$$

furthermore it yielded small metallic tin droplets after the experiment.

Regarding the spectra of the as-prepared samples, the modification by Pd leads both peaks to shift to lower temperature: the peak of surface species reduction is centered at 420 K and that of SnO_2 bulk reduction is at 760 K, while respective peaks of blank SnO_2 are centered at 500 K and 800 K, respectively. This indicates on the catalytic action of Pd in the processes of reduction with hydrogen. The low-temperature peak area, proportional to the amount of consumed H_2, is almost equal for both materials and corresponds to about 14.5 ± 0.5 μmol of O_2^- per 1 m^2 of samples surface. The O_2^- species were taken during this estimation solely for stoichometry simplicity to obtain some characteristic surface species concentration value. The assumption was based on the fact that it is O_2^- that was proved to be the predominant form of chemisorbed oxygen on tin dioxide at temperature below 430 K [1,17]. In our recent EPR study [18] of pure and modified nanocrystalline SnO_2 the surface O_2^- and OH radicals were

detected as the adsorbed derivatives of atmospheric oxygen and water. However, the Weisz limitation restricts the maximum ionic species concentration on the surface of semiconductors to about 10^{-3}–10^{-2} monolayer [17], which supposing the normal orientation of O_2^- and front radius close to O^- ionic radius (1.76 Å) corresponds to about 0.02–0.2 μmoles/m^2. As the value obtained from TPR-H_2 data exceeds the Weisz limit at least by two orders of magnitude, it is nessecarry to note that the actual surface species composition is far from the simplification used in the experimantal data treatment and besides the ionosorbates should include various neutral oxygen and hydroxyl derivatives with different stoichometry in H_2-reduction.

Not unexpectedly, the TPR-spectra of the samples after TPIE measurements exhibited a drastic drop in low-temperature H_2-consumption peak, that of SnO_2-TPIE sample being almost absent while in the spectrum of SnO_2/Pd-TPIE a low-intense broad line was observed in the 340–570 K range suggesting that some surface species concentration and/or Pd-induced catalytic action remained in the latter sample after high temperature treatment during TPIE. Taking into account that the Pd-modified sample is sintered to significantly lower extent than the blank SnO_2 sample, it seems reasonable that higher surface species concentration remains in the SnO_2/Pd sample due to its higher BET surface area. On the other hand, the high-temperature TPR peak due to bulk SnO_2 reduction shifts to higher temperature, but again to a different extent: for the SnO_2/Pd sample it is shifted from 760 K to 800 K, whereas for SnO_2 the shift from 800 K to 900 K was observed. The positive peak temperature shift for the processed materials could be due to increased crystallinity so that sintered materials have smaller surface energy and are less readily reducible by hydrogen. The difference in TPR temperature between the TPIE-tested samples could arise either from different crystallinity and/or from residual catalytic activity of palladium.

3.2. Kinetics of oxygen isotopic exchange in nanocrystalline SnO_2 and SnO_2/Pd

The raw data obtained during the TPIE experiments, i.e. molecular fractions of $^{16}O_2$, $^{18}O^{16}O$ and $^{18}O_2$ calculated by Eqs. (1)–(3) versus rising temperature, for the nanocrystalline SnO_2 and SnO_2/Pd samples are depicted in Fig. 6a and b, respectively. The starting temperature for oxygen isotopic exchange was recognized by the molecular oxygen fractions deviation from their initial values. Oxygen exchange starts from 700 K in blank SnO_2, while in the Pd-modified sample it starts from 590 K. Such essential temperature decrease is an evidence of the promotive effect of Pd on oxygen exchange in nanocrystalline tin dioxide. The ^{18}O atomic fraction calculated using Eq. (4) and molecular fraction f_{34} for blank and Pd-modified SnO_2 are shown in Figs. 7 and 8a, respectively. The ^{18}O atomic fraction decreases with the beginning of exchange suggesting heteroexchange as the predominant process in both samples.

On the basis of the reported data the total amount of substituted oxygen in the samples was estimated integrating the $\alpha(T)$ curves (Figs. 7 and 8a) according to the equation:

$$N(O_{exchanged}) = \frac{2}{V_m}\int_0^{t_{end}} \left(1-\frac{\alpha(t)}{\alpha_g^{input}}\right) F(t)dt, \quad (9)$$

where t is the time variable (min), t_{end} is the time of the experiment end (min), $\alpha(t)$ is the ^{18}O atomic fraction at the reactor outlet, α_g^{input} is the ^{18}O atomic fraction at the reactor inlet, $F(t)$ is the oxygen flow rate (l/min) and V_m is the molar gas volume. The estimated substituted oxygen amount was 7.9 mmol/g (60 at%) for SnO_2 and 7.0 mmol/g (54 at%) for SnO_2/Pd. It is necessary to note

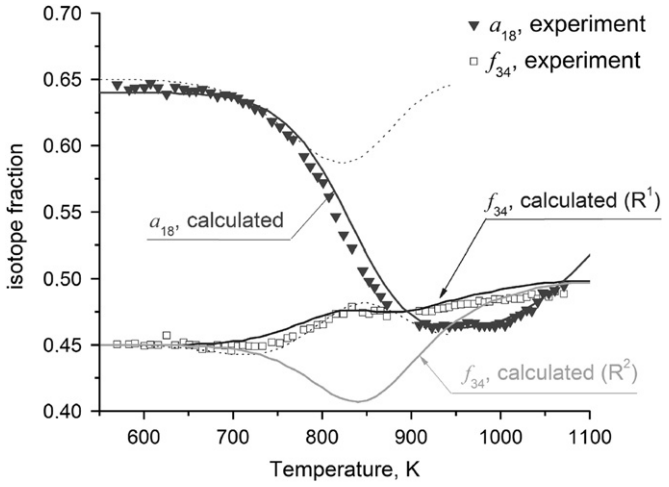

Fig. 7. Temperature dependence of ^{18}O isotope fraction (α_{18}: triangles—experimental values, line—simulation) and $^{18}O^{16}O$ molecules fraction (f_{34}: squares—experimental values, line—simulation) for SnO_2 sample. R^1 and R^2 designate simulated f_{34} curves in the frame of type I and type II heteroexchange models, respectively. Dotted line corresponds to the exchange of oxygen adsorbed on the surface of SnO_2.

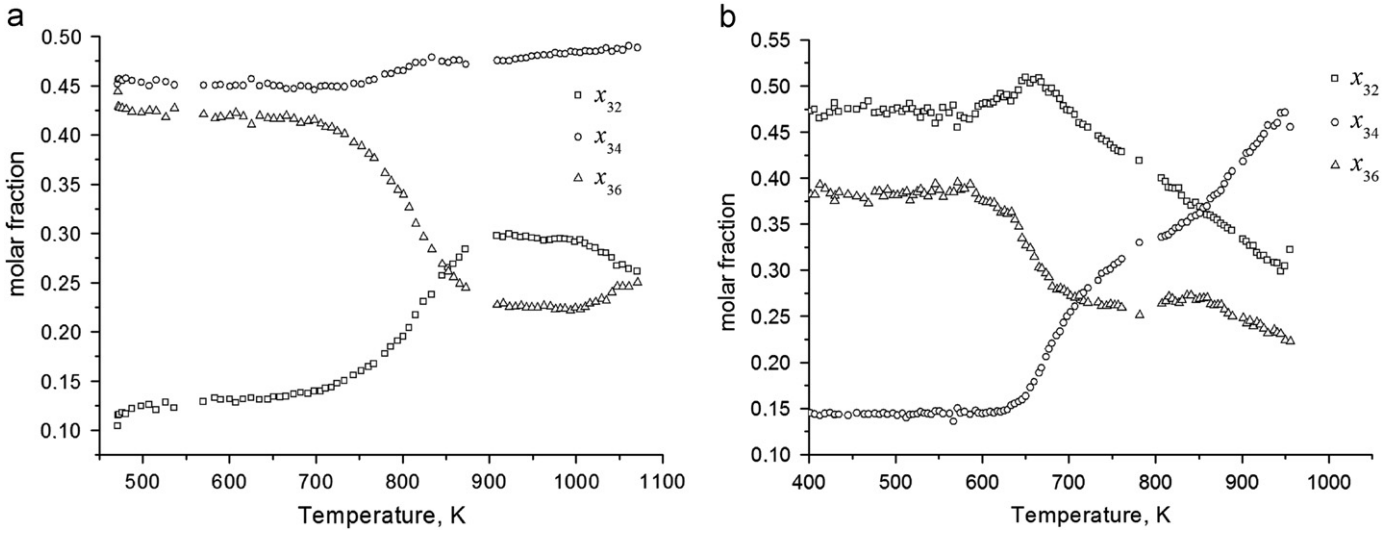

Fig. 6. Temperature dependences of molar fractions of $^{16}O_2$, $^{16}O^{18}O$ and $^{18}O_2$ in the outlet gas flow during TPIE experiments for SnO_2 (a) and SnO_2/Pd (b).

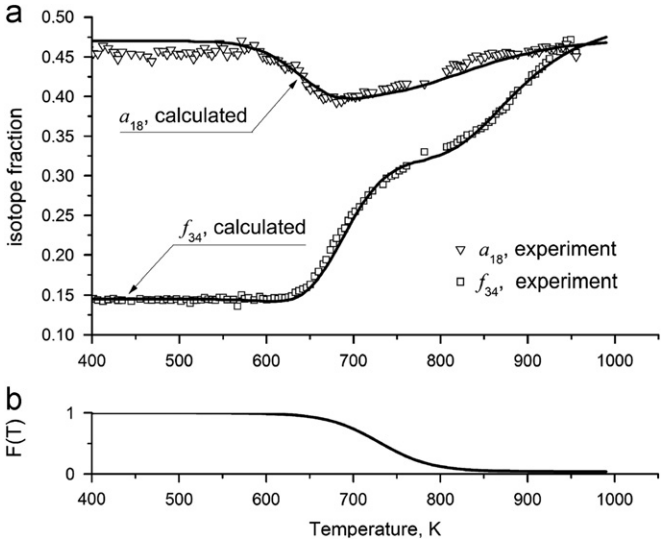

Fig. 8. (a) Temperature dependence of ^{18}O isotope fraction (α_{18}: triangles—experimental values, line—simulation) and $^{18}O^{16}O$ molecules fraction (f_{34}: squares—experimental values, line—simulation) for SnO_2/Pd sample. (b) The graph of empirical $F(T)$ function simulating active centers deactivation upon heating.

that substitution process was not completed in these experiments, i.e. ^{18}O isotope fraction in the outlet gas did not reach its value in the inlet gas. Hence, total exchangeable oxygen amount in the samples definitely exceeds the values obtained by integrating the experimental curves $\alpha(t)$.

3.3. Modeling the oxygen exchange

In general, three kinetically different types of isotope exchange (regarding the number of atoms from the solid being exchanged) are possible [19–21], namely

i) homoexchange without participation of oxygen atoms from the solid (type I according to the classification of Boreskov and Novakova [19,20], rate R^0):

$$^{18}O_2(g)+{}^{16}O_2(g)\leftrightarrow 2{}^{16}O{}^{18}O(g); \quad (10)$$

ii) simple heteroexchange between gas phase oxygen molecule and one oxygen atom from the solid (type II, rate R^1):

$$^{18}O_2(g)+{}^{16}O(s)\leftrightarrow {}^{16}O{}^{18}O(g)+{}^{18}O(s),$$

$$^{16}O{}^{18}O(g)+{}^{16}O(s)\leftrightarrow {}^{16}O_2(g)+{}^{18}O(s); \quad (12)$$

iii) multiple heteroexchange between gas phase oxygen molecule and two oxygen atoms of the solid (type III, rate R^2):

$$^{18}O_2(g)+2{}^{16}O(s)\leftrightarrow {}^{16}O_2(g)+2{}^{18}O(s), \quad (13)$$

$$^{18}O_2(g)+2{}^{16}O(s)\leftrightarrow {}^{16}O{}^{18}O(g)+{}^{16}O(s)+{}^{18}O(s), \quad (14)$$

$$^{16}O{}^{18}O(g)+2{}^{16}O(s)\leftrightarrow {}^{16}O_2(g)+{}^{16}O(s)+{}^{18}O(s). \quad (15)$$

Time variation of fractions of differently labeled oxygen molecules f_{32}, f_{34} and f_{36} is determined by the rates of all three types of exchange. The overall rate of heteroexchange $V=0.5R^1+R^2$ is the only factor determining the atomic fraction of ^{18}O in gas phase oxygen (α_g). In turn, the atomic fraction of ^{18}O within the surface layer of the oxide (α_s) depends on the rates of both heteroexchange on the oxide surface and labeled atoms transfer in the oxide bulk. The latter can be described by a diffusion equation proposed by Klier and Kucera [22] and Happel [23,24]. In the general case accounting for the three types of exchange the TPIE between gas phase oxygen and that in the oxide in the reactor can be modeled on the basis of the following mass balance equations:

$$C_{O_2}\left(\beta\frac{\partial\alpha_g}{\partial T}+\frac{1}{\tau}\frac{\partial\alpha_g}{\partial\xi}\right)=-b(0.5R^1+R^2)(\alpha_g-\alpha_s), \quad (16)$$

$$C_{O_2}\left(\beta\frac{\partial f_{34}}{\partial T}+\frac{1}{\tau}\frac{\partial f_{34}}{\partial\xi}\right)=bR^0(2\alpha_g(1-\alpha_g)-f_{34})+bR^1(\alpha_g(1-\alpha_s)+\alpha_s(1-\alpha_g)-f_{34})+bR^2(2\alpha_s(1-\alpha_s)-f_{34}), \quad (17)$$

$$\beta\frac{\partial\alpha_s}{\partial T}=(0.5R^1+R^2)(\alpha_g-\alpha_s)-\frac{N_{bulk}}{N_S}\frac{D}{h^2}\frac{\partial\alpha_{bulk}}{\partial\eta}\bigg|_{\eta=0}, \quad (18)$$

$$\beta\frac{\partial\alpha_{bulk}}{\partial T}=\frac{D}{h^2}\frac{\partial^2\alpha_{bulk}}{\partial\eta^2}. \quad (19)$$

Initial and boundary conditions

$$T=T_o: \quad \alpha_g=\alpha_g^{input},\ f_{34}=f_{34}^{input},\ \alpha_s=0,\ \alpha_{bulk}=0;$$

$$\xi=0: \quad \alpha_g=\alpha_g^{input},\ f_{34}=f_{34}^{input};$$

$$\eta=0: \quad \alpha_{bulk}=\alpha_s.$$

Here α_g, α_s and α_{bulk} are the atomic fractions of ^{18}O in gas phase oxygen, on the oxide surface and in the oxide bulk, respectively; f_{34} is the fraction of $^{16}O^{18}O$ molecule in gas phase; C_{O_2} is the gas phase oxygen concentration (mole/mole); τ is the residence time (s); b is the total number of surface sites (mole) per mole of gas molecules present in the catalyst section; R^0, R^1 and R^2 are the rates of different types of exchange as calculated per active site of the surface (s^{-1}); D is the diffusion coefficient of ^{18}O in the oxide bulk ($m^2\ s^{-1}$); h is the characteristic size of oxide particle (m), N_S and N_{bulk} is the numbers of oxygen atoms on the surface and in the oxide bulk, respectively; ξ is the dimensionless reactor length; η is the dimensionless depth of oxide layer, β is the heating rate; T is the reactor temperature.

The temperature dependences of oxygen exchange rates and diffusion coefficient were expressed by the Arrhenius equations:

$$R^{(i)}=R_{ref}^{(i)}\times e^{-(E_{R(i)}/RT)},\quad D=D_{ref}\times e^{-(E_D/RT)},\quad T'=\frac{TT_{ref}}{T_{ref}-T}, \quad (20)$$

where $R_{ref}^{(i)}$ and D_{ref} are exchange rate and diffusion coefficient at a reference temperature (T_{ref}) taken equal to 573 K, respectively; $E_{R(i)}$ and E_D are activation energies.

Fig. 7 illustrates the comparison of experimental $\alpha_g(T)$ and $f_{34}(T)$ curves for SnO_2 sample with the ones simulated on the basis of the model (16)–(20). Fitting distinguishes two possible types of heteroexchange. Being sensitive to the heteroexchange type, the $f_{34}(T)$ relation revealed the simple heteroexchange (see Fig. 7, curve R^1) as a predominant route of oxygen exchange in unmodified SnO_2.

The total number of exchangeable oxygen atoms in the oxide (N_s+N_{bulk}) estimated by this model is $N_O=6.7\times10^{21}$ atom/g, which is consistent with the stoichometric amount of oxygen in SnO_2 (8×10^{21} atom/g) taking into account the calculation errors.

The $\alpha_g(T)$ curve in Fig. 7 can be resolved into two overlapping peaks related to at least two states of oxygen in the oxide with different activities towards oxygen heteroexchange. The area of lower-temperature peak (Fig. 7, dotted line) corresponds to about $(1.6\pm0.4)\times10^{21}$ atom/g of exchangeable oxygen. An estimated lattice oxygen concentration in the surface layer of this sample is $(90\ m^2/g\times1.4\times10^{19}\ atom/g)\approx1.2\times10^{21}$ atom/g, as calculated for SnO_2(1 1 0) oxidized surface taking into account the BET surface area of the sample and lattice parameters of SnO_2 ($a=b=$ 4.7374 Å, $c=3.1864$ Å). These two oxygen atomic concentrations are quite close suggesting that it is surface oxygen exchange that is responsible for lower-temperature peak of $\alpha_g(T)$ curve in Fig. 7,

Table 1
Estimated kinetic parameters of oxygen exchange on SnO_2 and SnO_2/Pd.

Parameter[a]	Sample	
	SnO_2	SnO_2/Pd
R^1 (T=300 °C), $m^{-2}\,s^{-1}$	1.3×10^{12}	2.6×10^{12}
R^2 (T=300 °C), $m^{-2}\,s^{-1}$	None	5.7×10^{14}
D (T=300 °C), $m^{-2}\,s^{-1}$	6.1×10^{-24}	1.9×10^{-22}
$E(R^1)$, kJ/mole	130	130
$E(R^2)$, kJ/mole	None	110
$E(D)$, kJ/mole	80	80

[a] R^1—rate of simple heteroexchange, R^2—rate of multiple heteroexchange, D—oxygen bulk diffusion coefficient, E—corresponding activation energies.

while the higher-temperature peak must be due to the exchange of oxygen from grains bulk. Noteworthy, taking this assignment the fraction of exchangeable surface oxygen atoms from total number of exchangeable oxygen atoms is

$$\frac{N_s}{N_s+N_{bulk}}\approx\frac{1.6\cdot10^{21}\,\mathrm{atom/g}}{8.0\cdot10^{21}\,\mathrm{atom/g}}=0.2. \quad (21)$$

The kinetic parameters: heteroexchange rate, oxygen bulk diffusion coefficient at T_{ref} and corresponding activation energies evaluated and used in the simulation procedure are compared in Table 1.

The experimental $\alpha_g(T)$ and $f_{34}(T)$ data for Pd-modified SnO_2 could be adequately simulated (Fig. 8a) only if an additional type of exchange mechanism, namely multiple heteroexchange, is taken into account. It accounts for lower starting temperature of the process and describes the $\alpha_g(T)$ curve shape and initial $f_{34}(T)$ curve behavior at T=630–700 K. The kinetic parameters for both heteroexchange types and oxygen bulk diffusion for SnO_2/Pd are compared in Table 1. The strong promoting effect of Pd comprises the emergence of multiple heteroexchange stage with the rate by two orders of magnitude higher and activation energy by 20 kJ/mole lower than those of simple heteroexchange. It also addresses a 2-fold rise of the rate of type II heteroexchange and oxygen bulk diffusion coefficient increment by two orders of magnitude.

However, in the frame of Arrhenius law the S-shape bend observed for the $f_{34}(T)$ curve of SnO_2/Pd sample in the T=700–850 K region (Fig. 8a) could not be explained. Oxygen exchange in this case seems to be a rather complex process and to adequately fit the experimental curves $\alpha(T)$ and $f_{34}(T)$ in Fig. 8a the following function was proposed:

$$R^2(T)=R^2_{ref}e^{-(E_{R(i)}/RT')}\times F(T). \quad (22)$$

The decrease of oxygen exchange efficiency at 700–850 K evidenced by the bend is assumed to be due to active centers deactivation. The latter could arise from nanocrystals sintering and specific surface area decrease evidenced by XRD, BET and HRTEM analyses (Section 3.1) and from the catalyst deactivation. The Pd deactivation deduced also from the TPR-H_2 results (Section 3.1) could be due to the palladium sites decoration by agglomerated SnO_2 grains. Anyway, we propose an empirical $F(T)$ function (Fig. 8b) as a measure for the fraction of active centers on the surface of SnO_2/Pd for oxygen exchange. This relation was proposed to take into account the catalyst deactivation on raising the temperature when modeling the TPIE on SnO_2/Pd; it can be expressed by the following equation:

$$F(T)=1-0.95\frac{0.05\times\exp(-E_{deact}/RT'')}{1+0.05\times\exp(-E_{deact}/RT'')}\quad T''=\frac{TT_{deact}}{T_{deact}-T}. \quad (23)$$

Here T_{deact}=640 K is the temperature of the deactivation start; E_{deact}=140 kJ/mole can be regarded as an activation energy of this process.

3.4. Mechanism of oxygen exchange on SnO_2 and SnO_2/Pd

Simple heteroexchange (type II) usually proceeds via the Iley–Rideal mechanism involving direct oxygen molecule interaction with the surface oxide center. It is the exchange mechanism that was established for the SnO_2 sample. At the same time, multiple heteroexchange (type III), which is predominant for the SnO_2/Pd sample includes the preliminary oxygen molecule dissociation followed by the exchange of adsorbed oxygen atoms and lattice oxide ions. Earlier investigations of the oxygen exchange on oxide-supported noble metal particles [12,13] established that the latter tend to effect spill-over like activity in promoting oxygen exchange. Supposing similar behavior in the case of SnO_2/Pd and based on the interpretation provided by [12,13], the following reaction scheme can be suggested for the spill-over assisted exchange mechanism:

$^{18}O_{2(g)}\leftrightarrow2\,^{18}O_{(PdOx)}$ (dissociation);

$^{18}O_{(PdOx)}\leftrightarrow\,^{18}O_{(surf)}$ (spill-over);

$^{18}O_{(surf)}+\,^{16}O_{(bulk)}\leftrightarrow\,^{16}O_{(surf)}+\,^{18}O_{(bulk)}$ (exchange);

$^{16}O_{(surf)}\leftrightarrow\,^{16}O_{(PdOx)}$ (spill-over);

$^{18}O_{(PdOx)}+\,^{16}O_{(PdOx)}\leftrightarrow\,^{18}O^{16}O_{(g)}$ (recombination);

$2\,^{16}O_{(PdOx)}\leftrightarrow\,^{16}O_{2(g)}$ (recombination).

It is reasonable to assume that the dissociation rate of oxygen molecules is lower than the rate of atomic oxygen spill-over because of rather high O–O binding energy (493 kJ/mole [7]). Then the dissociation on the catalyst surface is a limiting stage, and this complex mechanism could be convoluted in a stage of multiple heteroexchange. Thus, for the SnO_2/Pd sample the oxygen exchange seems to be a combination of the simple heteroexchange (type II) mechanism like that in the case of blank SnO_2 and a multiple heteroexchange (type III) stage due to spill-over of atomic oxygen from palladium. This can be illustrated by the processes scheme in Fig. 9.

In the frame of these considerations on the oxygen exchange mechanism the Pd-induced increase of bulk diffusion coefficient (Table 1) can be accounted for. The samples under examination have a nanocrystalline structure; the atomic oxygen formed on the catalytic centers could be assumed to rapidly migrate via the intergrain boundaries and penetrate into the sample volume approaching the internal crystallites. In this case the promotion of surface diffusion would result in the enhancement of the apparent diffusion rate estimated from the experimental data. In this consideration Pd is believed to promote the oxygen surface diffusion due to the introduction of spill-over mechanism and increase of the heteroexchange rate. Noteworthy, similar phenomenon was previously observed in the work [12] for

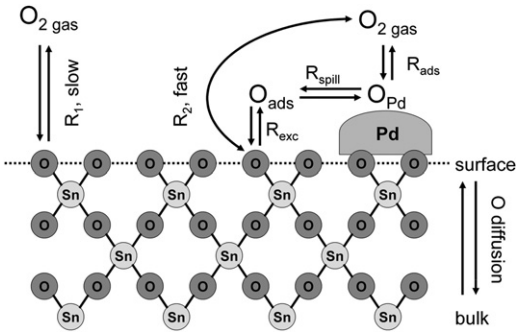

Fig. 9. Schematic illustration of the processes of oxygen exchange between palladium-modified tin dioxide and gas phase.

Pt-modified microcrystalline mixed oxides CeO_2–ZrO_2–La_2O_3. Oxygen transport mechanism in this type of materials including diffusion on the intergrain surface and diffusion into the grain bulk was also discussed in detail in [12].

Thus, the results of oxygen exchange study suggest that on unmodified SnO_2 oxygen is adsorbed in the molecular form. However, after the modification of SnO_2 by palladium the dissociation of O_2 on Pd centers followed by spill-over onto the support surface yields atomic oxygen. The modification of oxygen species on the surface of tin dioxide induced by palladium is an important factor that should not be underrated when considering the gas sensor performance of tin dioxide-based materials.

4. Conclusions

Temperature-programmed oxygen isotopic exchange study was performed for nanocrystalline blank and Pd-modified tin dioxide synthesized via aqueous deposition technique followed by impregnation with $Pd(acac)_2$ precursor and thermal treatment. Both materials were shown to exchange up to 100 at% of constituent oxygen via the heteroexchange route. The simple heteroexchange was established as the predominant mechanism of surface processes on SnO_2; the contributions from oxygen adsorbed on the surface and from the bulk of SnO_2 grains could be resolved. Tin dioxide modification by palladium brought up an exchange-promoting effect resulted in the following: (i) a decrease of the starting temperature of appreciable oxygen exchange; (ii) an introduction of multiple heteroexchange stage with higher exchange rate and lower activation energy, presumably due to spill-over action of Pd; (iii) a 100% increase of the rate of simple heteroexchange occurring due to SnO_2 support along with Pd-induced multiple heteroexchange; (iv) an increase by two orders of magnitude of the oxygen bulk diffusion coefficient. To account for the experimental data the catalyst deactivation process was assumed and modeled by a proposed empirical active centers fraction versus temperature dependence.

Supplementary material

HAADF-STEM image and EDX pattern of nanocrystalline SnO_2/Pd obtained from SnO_2 annealed at 573 K; HRTEM and HAADF-STEM micrographs of coarse SnO_2/Pd synthesized from SnO_2 annealed at 970 K visualizing Pd clustering on the surface of tin dioxide grains.

Acknowledgments

This work was supported by the Federal Science and Innovations Agency (state Contract no. 02.740.11.0139) and RFBR (Grants 11-03-00584-a and 09-03-01166-a).

Appendix A. Supplementary Information

Supplementary data associated with this article can be found in the online version at doi:10.1016/j.jssc.2011.11.028.

References

[1] M. Batzill, U. Diebold, Prog. Surf. Sci. 79 (2005) 47–154.
[2] R. Rella, P. Siciliano, S. Capone, M. Epifani, L. Vasanelli, A. Licciulli, Sens. Actuators B 58 (1999) 283–288.
[3] J. Kim, S.D. Han, I. Singh, H.D. Lee, J.S. Wang, Sens. Actuators B 107 (2005) 825–830.
[4] N.N. Samotaev, A.A. Vasiliev, B.I. Podlepetsky, A.V. Sokolov, A.V. Pisliakov, Sens. Actuators B 127 (2007) 242–247.
[5] Y.C. Lee, H. Huang, O.K. Tan, M.S. Tse, Sens. Actuators B 132 (2008) 239–242.
[6] M. Epifani, J. Arbiol, E. Pellicer, E. Comini, P. Siciliano, G. Faglia, J.R. Morante, Cryst. Growth Des. 8 (5) (2008) 1774–1778.
[7] G.C. Bond, C. Louis, D.T. Thompson, Catalysis by Gold, Imperial College Press, London, 2006.
[8] J. McAleer, P. Moseley, J. Norris, D. Williams, J. Chem. Soc. Faraday Trans. 83 (1987) 1323–1346.
[9] J.C. Belmonte, J. Manzano, J. Arbiol, A. Cirera, J. Puigcorbe, A. Vila, N. Sabate, I. Gracia, C. Cane, J.R. Morante, Sens. Actuators B 114 (2006) 881–892.
[10] S. Harbeck, A. Szatvanyi, N. Barsan, U. Weimar, V. Hoffmann, Thin Solid Films 436 (2003) 76–83.
[11] A.V. Marikutsa, M.N. Rumyantseva, L.V. Yashina, A.M. Gaskov, Solid State Chem. 183 (2010) 2389–2399.
[12] E.M. Sadovskaya, Y.A. Ivanova, L.G. Pinaeva, G. Grasso, T.G. Kuznetsova, A. van Veen, V.A. Sadykov, C. Mirodatos, J. Phys. Chem. 111 (2007) 4498–4505.
[13] C. Descorme, D. Duprez, Appl. Catal. A: Gen. 202 (2000) 231–237.
[14] I.K. Murwani, S. Scheurell, M. Feist, E. Kemnitz, J. Therm. Anal. Cal. 69 (2002) 9–21.
[15] K. Scheurell, E. Hoppe, K. Brzezinka, E. Kemnitz, J. Mater. Chem. 14 (2004) 2560–2568.
[16] O.V. Safonova, M.N. Rumyantseva, L.I. Ryabova, M. Labeau, G. Delabouglise, A.M. Gaskov, J. Mater. Sci. Eng. B 85 (2001) 43–49.
[17] C.O. Park, S.A. Akbar, J. Mater. Sci. 38 (2003) 4611–4637.
[18] A.V. Marikutsa, M.N. Rumyantseva, A.M. Gaskov, E.A. Konstantinova, D.A. Grishina, D.M. Deygen, Thin Solid Films 520 (2011) 904–908.
[19] G.K. Boreskov, Adv. Catal. 15 (1964) 285–339.
[20] J. Novakova, Catal. Rev. 4 (1970) 77–114.
[21] A. Ozaki, Isotopic Studies of Heterogeneous Catalysis, Academic Press, New York, 1977.
[22] K. Klier, E. Kucera, J. Phys. Chem. Solids 27 (1966) 1087–1095.
[23] J. Happel, E. Walter, Y. Lecourtier, J. Catal. 123 (1990) 12–20.
[24] E. Walter, L. Pronzato, Y. Soong, M. Otarod, J. Happel, J. Ind. Eng. Chem. Res. 34 (2) (1995) 483–491.